UC Davis
UC Davis Previously Published Works

Title

Steering CO2 hydrogenation toward C-C coupling to hydrocarbons using porous organic polymer/metal interfaces.

Permalink

Journal

Authors

Zhou, Chengshuang
Asundi, Arun
Goodman, Emmett
et al.

Publication Date

DOI

Steering CO_2 hydrogenation toward C–C coupling to hydrocarbons using porous organic polymer/metal interfaces

Chengshuang Zhou[a] , Arun S. Asundi[a,b], Emmett D. Goodman[a,b], Jiyun Hong[c], Baraa Werghi[a,b,c] , Adam S. Hoffman[c], Sindhu S. Nathan[a,b] , Stacey F. Bent[a,b], Simon R. Bare[b,c] , and Matteo Cargnello[a,b,1]

[a]Department of Chemical Engineering, Stanford University, Stanford, CA 94305; [b]SUNCAT Center for Interface Science and Catalysis, Stanford University, Stanford, CA 94305; and [c]Stanford Synchrotron Radiation Lightsource, SLAC National Accelerator Laboratory, Menlo Park, CA 94025

The conversion of CO_2 into fuels and chemicals is an attractive option for mitigating CO_2 emissions. Controlling the selectivity of this process is beneficial to produce desirable liquid fuels, but C–C coupling is a limiting step in the reaction that requires high pressures. Here, we propose a strategy to favor C–C coupling on a supported Ru/TiO_2 catalyst by encapsulating it within the polymer layers of an imine-based porous organic polymer that controls its selectivity. Such polymer confinement modifies the CO_2 hydrogenation behavior of the Ru surface, significantly enhancing the C_{2+} production turnover frequency by 10-fold. We demonstrate that the polymer layers affect the adsorption of reactants and intermediates while being stable under the demanding reaction conditions. Our findings highlight the promising opportunity of using polymer/metal interfaces for the rational engineering of active sites and as a general tool for controlling selective transformations in supported catalyst systems.

CO_2 hydrogenation | C–C coupling | polymer/metal interface

With the pressing environmental challenges imposed by CO_2 emissions, efforts must be devoted to mitigating them (1). Hydrogenation of captured CO_2 into valuable chemicals offers this opportunity while also reducing our dependence on fossil fuels (2). The catalytic transformation of CO_2 into C_1 products (carbon monoxide, methane, methanol, and formic acid) has been extensively studied with remarkable progress (3), but these molecules suffer from lower specific energy density compared to higher-molecular-weight hydrocarbons (C_{2+}). Engineering of active sites plays a crucial role in increasing the C/H ratio on the catalyst surface and thus enhancing the coupling probability. While progress in the synergistic stepwise conversion of CO_2 to hydrocarbons has led to C_{2+} products (4, 5), less has been achieved in affecting the reactivity of pristine metal surfaces toward improving direct C–C coupling selectivity.

It is well accepted that local interactions, such as metal–support or metal–ligand interactions, determine the binding strength of reaction intermediates that affect product distribution (6). Indeed, as predicted by scaling relationships, the binding strength of appropriate intermediates is directly related to reaction rates, and they can be used to tune reaction selectivity (7). As an example, the reactivity of TiO_2-supported Rh catalysts can be switched from methanation to reverse water gas shift (RWGS) when an adsorbate-mediated strong metal–support interaction overlayer is formed under reaction conditions (8). This layer weakens CO binding and drastically alters the reaction selectivity, thus demonstrating how overlayers can tune surface reactivity in a potentially predictable way.

Modifying active sites with organic ligands offers a promising approach to tune the binding of reactants and intermediates thanks to the wide range of chemical functional groups that can be introduced using organic components (9–12). For CO_2

hydrogenation in particular, Medlin and coworkers showed how the selectivity toward RWGS can be significantly enhanced on Pt/TiO_2 and Pd/TiO_2 catalysts through TiO_2 surface modification with molecular ligands. The inclusion of amino groups notably promoted CO_2 activation and increased rates (13).

Owing to their tunable pore structure and richness in chemical functionality, porous organic polymers provide many opportunities for catalyst surface modification, with strong potential in hierarchical pore construction (14), linkage composition (15), morphology engineering (16), and tuning of catalytic properties (17). Most importantly, polymers with amine or imine functionality have been proven able to adsorb and activate CO_2 (18, 19). We therefore hypothesize that these materials could modify the surface reactivity of metals embedded within the polymer pore structure in activating CO_2. We thus report the uniform encapsulation of a Ru/TiO_2 supported catalyst within a tunable layer of an imine-based porous organic polymer (IPOP) with controllable morphology and chemical functionality. Such polymer confinement modifies the CO_2 hydrogenation behavior of the Ru surface, significantly enhancing the C_{2+} production turnover frequency (TOF), whereas the starting Ru/TiO_2 makes mostly methane. Kinetic measurements demonstrate an 80-fold and 10-fold increase in the CO and C_{2+} production TOF, respectively, with the IPOP coating. We further demonstrate that the polymer effect on selectivity is general and occurs on several Ru/metal oxide supported catalysts

---

Significance

In the field of CO_2 conversion, a crucial reaction for a sustainable future, controlling the selectivity to improve C–C coupling to higher products is challenging because of the notorious inertness of CO_2 and the stepwise conversion that occurs on conventional catalysts. Here, we show that porous polymer encapsulation of metal-supported catalysts is capable of driving the selectivity in the CO_2 conversion to hydrocarbons. With this strategy, we achieve an outstanding improvement in C–C coupling that results in orders of magnitude higher turnover frequencies for hydrocarbon formation compared to conventional catalysts.

CHEMISTRY

and with a similar magnitude of selectivity control. Such polymer-induced reactivity control provides promising opportunities for the rational engineering of active sites not only for CO_2 conversion but as a general tool for other selective transformations using supported catalysts.

Results and Discussion

Synthesis and Characterization of IPOP/Ru/TiO₂ Hybrid Catalyst.
The design of organic/inorganic hybrids involved multiple sequential steps such that the individual components could be easily tuned (Scheme 1). To synthesize the IPOP/Ru/TiO₂ hybrid catalysts, a Ru/TiO₂ sample was first prepared by deposition of colloidal Ru nanoparticles on a commercial titania support (20). The Ru/TiO₂ was then used as a template for solution-phase polymer growth based on imine condensation reaction between 1,3,5-Tris(4-aminophenyl)benzene and terephthalaldehyde (or paraphthalaldehyde, p-PA) to form p-IPOP (Scheme 1).

Transmission electron microscopy (TEM) was used to characterize the morphology of as-synthesized catalysts and examine the degree of encapsulation. Fig. 1*A* and *SI Appendix*, Fig. S1 show ~3 nm Ru nanoparticles supported on TiO₂ crystallites in the Ru/TiO₂ sample. After IPOP growth, a low-contrast material uniformly surrounds the Ru/TiO₂ particles in the IPOP/Ru/TiO₂ sample (Fig. 1*B*). High-resolution imaging demonstrates that the layer is not crystalline and that it homogeneously coats the whole surface, with an average thickness of ~15 nm (Fig. 1*C*).

Energy-dispersive X-ray scattering (EDS) analysis of the p-IPOP/Ru/TiO₂ sample was performed on high-angle annular dark-field scanning TEM (HAADF-STEM) images to map the spatial distribution of the elements (Fig. 1*D*), which show brighter areas corresponding to the Ru/TiO₂ catalyst particles enveloped in a low-contrast overlayer. By comparing the STEM image and the corresponding EDS maps (Fig. 1 *E–G*), it is found that nitrogen from IPOP is present across the image, while Ti and Ru are evident only in the interior of the grains. Thus, we conclude that Ru/TiO₂ is uniformly surrounded by the nitrogen-rich IPOP.

As in Fig. 2*A*, X-ray photoelectron spectroscopy (XPS) was also collected but the Ru signal is hardly distinguishable even in the bare Ru/TiO₂ due to both the low concentration of Ru
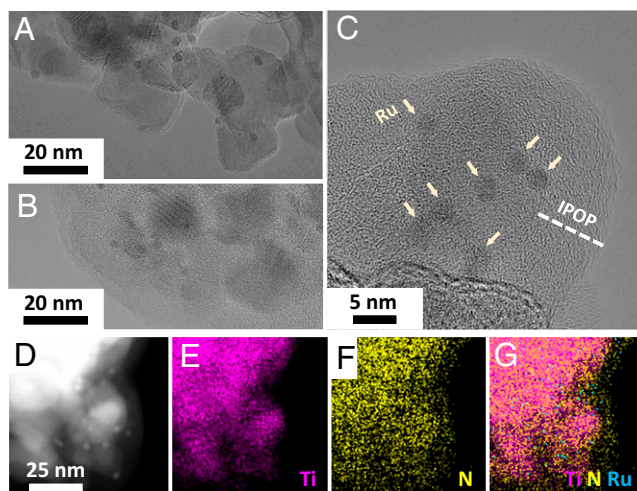

Fig. 1. Characterization of the hybrid IPOP/Ru/TiO₂ catalyst. (*A*) Representative TEM image of pristine Ru/TiO₂. Note that the TiO₂ particles show rough edges induced by the electron beam. (*B*) Representative TEM and (*C*) high-resolution TEM images of p-IPOP/Ru/TiO₂. Arrows and lines were intentionally added to highlight individual components. (*D*) Representative STEM image and (*E–G*) corresponding EDS maps of Ti, N, and Ru elements in the p-IPOP/Ru/TiO₂ sample.

present and the overlap between the Ru 3d peak (~279 eV for Ru $3d_{5/2}$ and ~284 eV for Ru $3d_{3/2}$) and the C 1s peak (284.8 eV). Only adventitious carbon is found in Ru/TiO₂, while p-IPOP/Ru/TiO₂ shows signals that are consistent with a carbon framework (284.8 eV) as well as carbon atoms bonded to nitrogen atoms (286.5 eV), both of which originate from the IPOP. An additional weak signal at 290.8 eV in the p-IPOP/Ru/TiO₂ sample is attributed to the π–π conjugation of stacked aromatic rings in the IPOP. The Ti signal could be well-distinguished in the Ru/TiO₂ sample and was consistent with Ti(IV) in TiO₂ (Fig. 2*B*). The Ti signal in the IPOP/Ru/TiO₂ catalyst, however, is significantly attenuated and almost indistinguishable from the baseline, proving the encapsulation of the Ru/TiO₂ material within IPOP layers at least 5 to 10 nm thick that prevents the escape of photoemitted electrons.
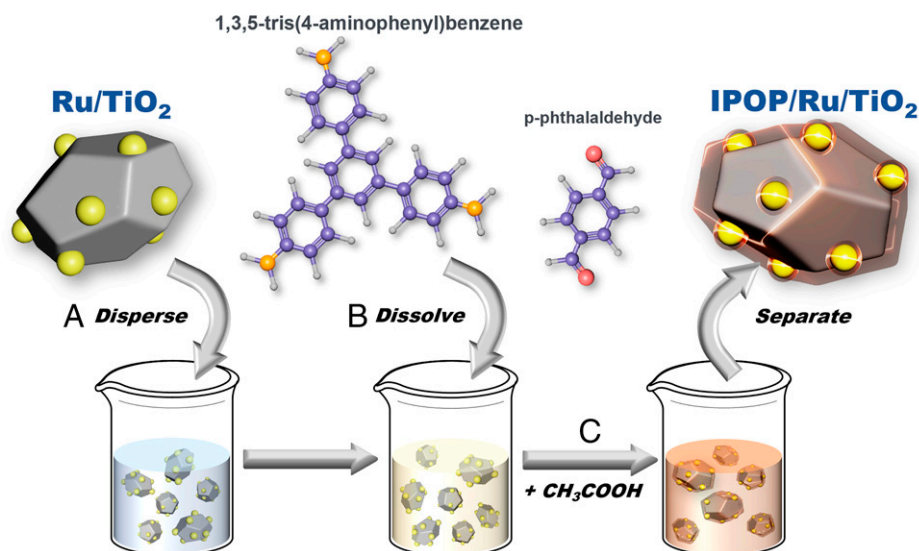
Scheme 1. Schematic of the synthesis process. Synthesis of IPOP/Ru/TiO₂ by encapsulation of Ru/TiO₂ within IPOP through dispersion of the Ru/TiO₂ sample (*A*), addition of IPOP precursors (*B*), and acid-catalyzed imine network formation (*C*).
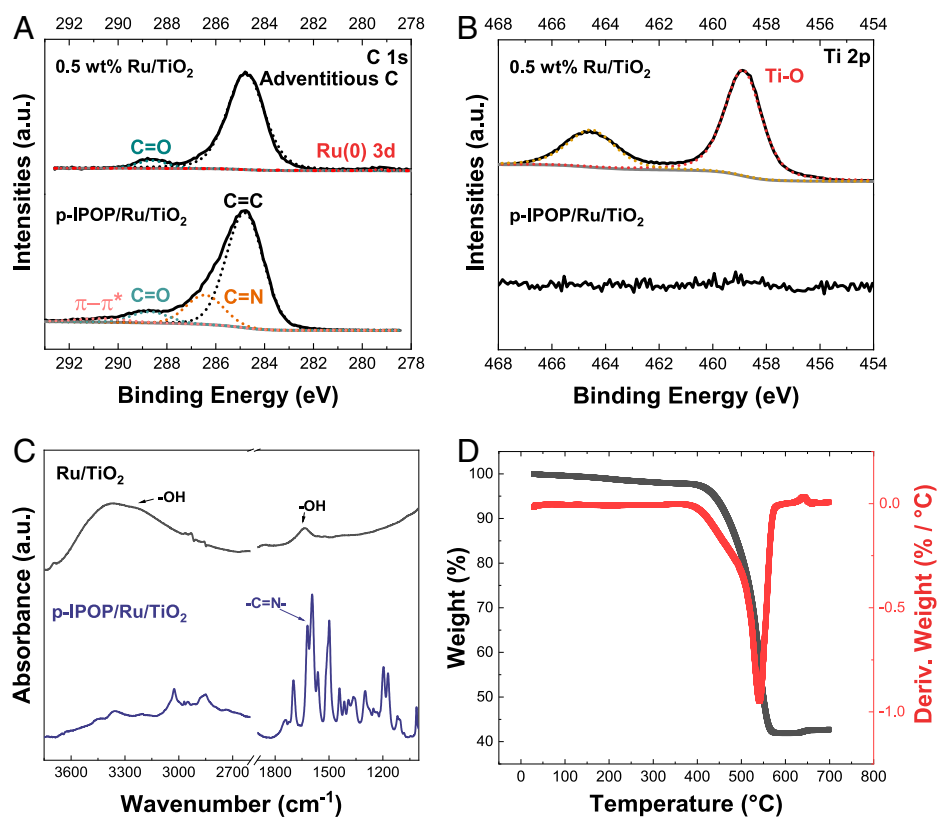
Fig. 2. Characterization of the catalysts. (*A*) C 1s and (*B*) Ti 2p XPS spectra of Ru/TiO₂ and p-IPOP/Ru/TiO₂. (*C*) FTIR spectrum of Ru/TiO₂ and p-IPOP/Ru/TiO₂. (*D*) Thermogravimetric analysis of p-IPOP/Ru/TiO₂.

The synthesis method could be extended to other polymer compositions starting from either *ortho*-phthalaldehyde (*o*-PA) or metaphthalaldehyde (m-PA), resulting in the formation of *o*-IPOP/Ru/TiO₂ and m-IPOP/Ru/TiO₂. Such a family of polymer-encapsulated samples differs in the connectivity of polymer-building units. Characterization of the samples revealed the uniform encapsulation with comparable thickness and similar morphology to the p-IPOP/Ru/TiO₂ sample (*SI Appendix*, Figs. S2–S4).

Fourier transform infrared (FTIR) spectroscopy analysis confirmed the presence of hydroxyl groups in the Ru/TiO₂ sample evidenced by broad vibrational modes at ~1,635 cm⁻¹ and ~3,350 cm⁻¹ (Fig. 2*C*). Such peaks are absent in the p-IPOP/Ru/TiO₂ sample, where the TiO₂ surface is instead covered by p-IPOP showing characteristic vibrations from the polymer including the C=N bond contribution at ~1,620 cm⁻¹. Similar spectra were collected for *o*-IPOP/Ru/TiO₂ and m-IPOP/Ru/TiO₂ (*SI Appendix*, Fig. S6). We hypothesize that surface hydroxyls on TiO₂ act as anchoring groups for IPOP growth, favoring imine condensation on the surface without any additives and resulting in uniform polymer encapsulation (21). Indeed, when TiO₂ was calcined to remove hydroxyl groups, IPOP nucleated in solution (*SI Appendix*, Fig. S5*A*) (22), whereas when the TiO₂ was rehydroxylated then uniform encapsulation could be achieved again (*SI Appendix*, Fig. S5 *B* and *C*).

Thermogravimetric analysis of the p-IPOP/Ru/TiO₂ catalyst showed minimal mass loss in airflow up to 400 °C (Fig. 2*D*), thus demonstrating the polymer's stability even in the presence of Ru/TiO₂. The polymer started to degrade above 400 °C (23). Temperature-programmed reduction experiments of p-IPOP/Ru/TiO₂ further demonstrated the excellent stability of the sample up to 350 °C under conditions more relevant for catalytic hydrogenation (*SI Appendix*, Fig. S7). Similar thermal

stability was also found with *o*- and m-IPOP/Ru/TiO₂ samples, although m-IPOP/Ru/TiO₂ started to degrade above 350 °C, likely due to a lower degree of polymerization (*SI Appendix*, Fig. S8).

The p-IPOP layers significantly increased the surface area of Ru/TiO₂ with the introduction of both micro- and mesoporosity (*SI Appendix*, Fig. S9). The BET surface area increased from 56 m²·g⁻¹ for bare Ru/TiO₂ to 222 m²·g⁻¹ in p-IPOP/Ru/TiO₂. The three polymer isomers were not equally porous (88 and 54 m²·g⁻¹ for *o*- and m-IPOP/Ru/TiO₂, respectively), likely because of the different conformation obtained with *o*-, m-, and p-phthalaldehyde in the final IPOP layers.

CO₂ Hydrogenation on IPOP/Ru/TiO₂ Hybrid Catalysts. The catalysts were tested for CO₂ hydrogenation to evaluate the effect of polymer layers on the catalytic performance of Ru/TiO₂. CO₂ conversions were approximately the same and, in most cases, intentionally kept below 6% to compare selectivity in a kinetically controlled regime.

The reaction was initially performed at atmospheric pressure (*SI Appendix*, Fig. S10). The Ru/TiO₂ sample produced methane with 98% selectivity, in agreement with previous reports (24–27). The p-IPOP/Ru/TiO₂ sample, however, showed dramatically different selectivity with nearly 100% CO selectivity. Such reversal in selectivity from methanation to RWGS has been previously reported in Pt and Pd catalysts modified with phosphonic acid ligands (13). However, Ru favors methanation more strongly than Pd and Pt. This change in selectivity is therefore unique for Ru nanoparticles [not to be confused with Ru single atoms (20) or clusters (28) which contain Ru^δ+ species] irrespective of the support nature (24–27, 29).

The catalysts were then tested at 6 bar of pressure. The increased pressure did not significantly change the product

Zhou et al.
Steering CO₂ hydrogenation toward C–C coupling to hydrocarbons using porous organic polymer/metal interfaces

PNAS | 3 of 10
https://doi.org/10.1073/pnas.2114768119

Table 1. Apparent activation energy and partial reaction orders of the different catalysts

	$E_{a,CO}$, kJ·mol^{-1}	$E_{a,CH4}$, kJ·mol^{-1}	$R_{CO} \propto p_{H_2}{}^x$	$R_{CO} \propto p_{CO_2}{}^x$	$R_{CH_4} \propto p_{H_2}{}^x$	$R_{CH_4} \propto p_{CO_2}{}^x$
Ru/TiO$_2$	69 ± 4	88 ± 1	−0.5 ± 0.1	1.6 ± 0.1	0.4 ± 0.1	0.7 ± 0.1
o−IPOP/Ru/TiO$_2$	74 ± 7	58 ± 1	−0.4 ± 0.1	1.1 ± 0.1	1.3 ± 0.1	0.5 ± 0.1
m−IPOP/Ru/TiO$_2$	88 ± 2	61 ± 1	−0.5 ± 0.1	1.1 ± 0.1	1.4 ± 0.1	0.7 ± 0.1
p−IPOP/Ru/TiO$_2$	90 ± 2	69 ± 2	−0.4 ± 0.1	1.3 ± 0.1	1.5 ± 0.1	0.5 ± 0.1

For apparent activation energy calculation, CO_2 hydrogenation was carried out under 20 sccm 75% H_2 + 25% CO_2, 6 bar total pressure, at temperatures of 220, 230, 240 and 250 °C. Rate order measurements were carried out at 250 °C, 6 bar total pressure. To calculate CO_2 rate order, H_2 pressure was kept at 75% while CO_2 pressure was varied from 15 to 25% with 1% interval. To calculate H_2 rate order, CO_2 pressure was kept at 15% while H_2 pressure was varied from 45 to 80% with 4% interval.

distribution of the Ru/TiO$_2$ sample where methane formation was favored in 99% yield, while also producing some C_{2+} hydrocarbons in very low yield (Fig. 3*A*). However, C_{2+} hydrocarbon production was dramatically enhanced on the IPOP-encapsulated samples, with a pronounced steady increase in C_{2+} selectivity from Ru/TiO$_2$ (<1%), to o-IPOP/Ru/TiO$_2$ (1%), to m-IPOP/Ru/TiO$_2$ (5%), to p-IPOP/Ru/TiO$_2$ (12%). As opposed to low pressure, all the IPOP-encapsulated samples also showed increased production of methane, with selectivity steadily decreasing from o-IPOP/Ru/TiO$_2$ (96%), to m-IPOP/Ru/TiO$_2$ (92%), to p-IPOP/Ru/TiO$_2$ (64%).

When either CO_2 or H_2 was removed from the reactant feed and replaced by inert gas, hydrocarbon formation instantaneously ceased (*SI Appendix*, Fig. S11), indicating that the hydrocarbon species are produced by the conversion of CO_2 and H_2 on the catalyst surface. The TOFs for hydrocarbon production were calculated based on CO chemisorption measurements (Fig. 3*B* and *SI Appendix*, Table S1). CO production was significantly promoted by 50- to 80-fold on all three IPOP-encapsulated catalysts compared to the Ru/TiO$_2$ sample, in agreement with ambient pressure experiments (*SI Appendix*, Fig. S10). The C_1–C_4 hydrocarbon yield was also enhanced by

IPOP encapsulation to different degrees for the polymer isomers. Note that such enhancement in TOF and selectivity could not simply originate from physical blockage by the polymer (*SI Appendix*, Table S3). The α parameter, which describes the probability of *C intermediates to form C–C bonds, was calculated from Anderson–Shulz–Flory theory and compared among catalysts (Fig. 3*B*) (4). It steadily increased from the Ru/TiO$_2$ sample (α = 0.08) to the polymer-coated catalysts to a value of 0.39 for the p-IPOP/Ru/TiO$_2$ catalyst. This result demonstrates that polymer encapsulation significantly increases the probability of C–C coupling and hydrocarbon production, which is rarely reported on Ru-based catalysts under the mild pressure conditions used in this work (2, 30–32).

Mechanistic Studies of CO_2 Hydrogenation at IPOP/Metal Interfaces. Kinetic parameters, including apparent activation energy and reaction rate orders, were collected and are summarized in Table 1. Apparent activation energy for CH_4 or CO formation ($E_{a,CH4}$ and $E_{a,CO}$) at 6 bar on Ru/TiO$_2$ was 88 ± 1 and 69 ± 4 kJ·mol^{-1}, respectively (*SI Appendix*, Fig. S12), the former in line with previous reports (20, 27, 32, 33), while the latter is not usually reported for Ru catalysts. Since RWGS and methanation
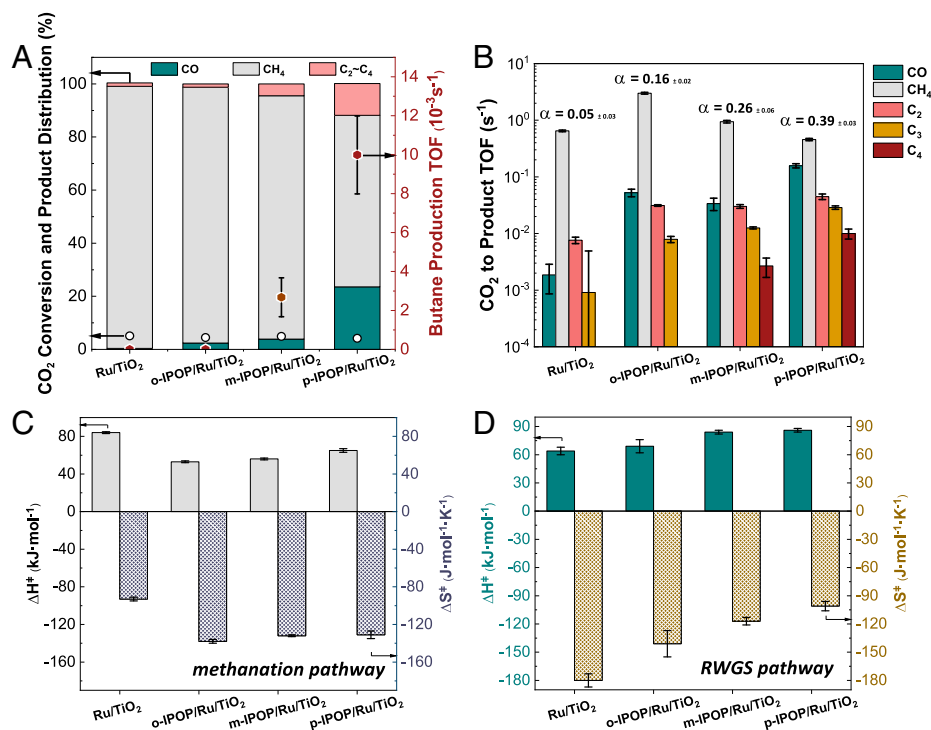

Fig. 3. Catalytic reactivity of Ru/TiO$_2$ and IPOP/Ru/TiO$_2$ samples. (*A*) Conversion and product distributions for CO_2 hydrogenation at 250 °C, 30 sccm 75% H_2 + 25% CO_2, 6 bar total pressure and (*B*) corresponding reaction TOFs for different catalysts. Transition-state enthalpy and entropy, respectively, for (*C*) methanation and (*D*) RWGS pathways of different catalysts.

pathways share similar intermediate steps (28, 34, 35), close values for the activation energies are reasonable. $E_{a,CH4}$ for IPOP-coated catalysts also showed values between 58 and 69 $kJ \cdot mol^{-1}$. On the other hand, the activation energies for CO formation were quite different (75 to 92 $kJ \cdot mol^{-1}$), which suggests that IPOP encapsulation induces changes in the RWGS pathway.

The transition state enthalpy ($\Delta H^{\ddagger}$) and entropy ($\Delta S^{\ddagger}$) values extracted from Eyring plots compensate each other for the methanation reaction on all the catalysts (see calculation steps in *Materials and Methods*, Fig. 3*C*, and *SI Appendix*, Fig. S13). This result is not surprising given that the intrinsic reaction rates for methane formation were similar (Fig. 3*B*). However, the situation is very different for CO formation through RWGS reaction (Fig. 3*D*). Transition-state enthalpy values increased from Ru/TiO_2 to o-, m-, and p-IPOP/Ru/TiO_2 with a concomitant similar trend in the activation entropy values increasing from very negative for Ru/TiO_2 (-180 ± 7 $J \cdot mol^{-1} \cdot K^{-1}$) to less and less negative for o-, m-, and p-IPOP/Ru/TiO_2 samples (-141 ± 14, -117 ± 4, and -101 ± 5 $J \cdot mol^{-1} \cdot K^{-1}$, respectively), thus highlighting how the transition state is less strongly adsorbed on the Ru surface but has higher degree of freedom potentially by interacting with the IPOP layers. Such favorable entropic contribution induced by polymer encapsulation compensates for the milder increase in transition-state enthalpy and explains the significantly increased CO production in the IPOP-encapsulated catalysts. Moreover, the trend strongly suggests that the IPOP layers distinguishably affect the reaction pathway and energy landscape through active interactions with the transition states in a manner analogous to previous reports (36).

The rate of methane production over Ru/TiO_2 catalyst showed moderate dependence on CO_2 ($+0.7 \pm 0.1$) and weak dependence on H_2 ($+0.4 \pm 0.1$) (*SI Appendix*, Figs. S14 and S15), suggesting that the Ru surface is mostly covered by hydrogen instead of carbon species (33, 37). The rate orders for RWGS reaction are very different from those of methanation, with strong dependence on CO_2 ($+1.6 \pm 0.1$) and negative dependence on H_2 (-0.5 ± 0.1). The notably more negative hydrogen rate order compared to methanation indicates that the two reactions proceed through competitive pathways. It has been reported that a high C/H ratio on the Ru surface is favorable for C–C coupling, while a low ratio leads to methane formation (2, 31, 38). The low C/H ratio indicated by the CO_2 and H_2 pressure dependence in Ru/TiO_2 therefore supports the high methanation selectivity. Instead, it was found that IPOP-encapsulated catalysts have surprisingly higher hydrogen rate orders (1.3 to 1.5) at the same comparable CO_2 rate order (0.5 to 0.7) (*SI Appendix*, Figs. S14 and S15). Combined with the notably enhanced C_{2+} selectivity, it is hypothesized that polymer encapsulation affects the hydrogen adsorption on the Ru surface, increasing the H_2 dependence and C/H ratio and promoting C–C coupling. Meanwhile, unlike the case of methanation, the IPOP layers did not induce notable differences in RWGS rate orders, which again suggests that RWGS and methanation undergo separate pathways over encapsulated catalysts. In summary, kinetic analysis suggests that the IPOP layers actively interact with reaction intermediates, modifying the concentration of adsorbate species on the Ru surface and increasing the C/H ratio, heavily favoring C_{2+} production.

Diffuse reflectance infrared Fourier transform spectroscopy (DRIFTS) using CO as a probe molecule for both RWGS and methanation pathways was performed to gain information on reaction intermediates. In the case of Ru/TiO_2, overlapping adsorption peaks centered around 2,066 cm^{-1} and 1,998 cm^{-1} arose upon the introduction of CO at room temperature and ambient pressure (Fig. 4*A*). After gaseous CO removal by vacuum, four sets of peaks could be discerned at 2,137 cm^{-1}, 2,077 cm^{-1}, 2,059 cm^{-1}, and 1,972 cm^{-1} attributed to multicarbonyl species adsorbed on partially oxidized Ru crystallites for

the former two, linear CO adsorbed on extended Ru surfaces for the third (35, 39, 40), and CO adsorbed on Ru defects (41), partially oxidized Ru (39, 40), or in general Ru atoms in contact with the TiO_2 support [CO-Ru(TiO_2)] for the latter (39, 40). When the temperature was gradually increased to 250 °C, the frequency of the $(CO)_n$-$Ru^{\delta+}$ peaks at 2,137 cm^{-1} and 2,077 cm^{-1} did not change, suggesting that CO adsorption at these sites is not sensitive to coverage. It is proposed that dissociative CO adsorption into C and O is responsible for these slightly oxidized Ru sites (35, 39, 40). On the contrary, the peak at 2,059 cm^{-1} gradually shifted to 2,006 cm^{-1} as temperature was increased to 250 °C, likely due to the decreased coverage of adsorbed CO. Ru/TiO_2 has strong binding affinity for CO, and CO partially dissociates instead of desorbing upon heating, favoring its conversion to methane.

In the case of the p-IPOP/Ru/TiO_2 sample, a CO adsorption peak centered at ∼2,042 cm^{-1} could also be discerned upon introduction of CO at room temperature and ambient pressure. The peak shifted to 1,966 cm^{-1} under vacuum and disappeared upon moderate heating to ∼100 °C, evidencing that CO adsorbs weakly when the polymer layers are present. The same labile CO adsorption was found on o-IPOP/Ru/TiO_2 and m-IPOP/Ru/TiO_2 catalysts (*SI Appendix*, Fig. S16). This behavior explains the 100% RWGS selectivity at ambient pressure, as any *CO intermediate feasibly desorbs from the Ru surface before undergoing further hydrogenation to methane.

CO DRIFTS at higher pressure was then investigated on p-IPOP/Ru/TiO_2 (*SI Appendix*, Fig. S17). At 250 °C, an adsorption peak attributable to linear CO on Ru_x sites was found at ∼1,986 cm^{-1}, and its intensity positively correlated with increasing CO partial pressure. This observation suggests that CO adsorption can be increased with external pressure, thus making the sample more reactive, which is consistent with the hydrocarbon production results obtained for this sample at higher pressure (Fig. 3*A* and *SI Appendix*, Fig. S10).

Finally, *operando* DRIFT spectra were collected under reaction conditions at 6 bar of pressure (Fig. 4 *B* and *C*). For Ru/TiO_2 (Fig. 4*B*), multiple species were formed upon the introduction of CO_2 together with contributions from gaseous H_2O which appear as sharp peaks due to their rotational components. The broad features at 1,880 to 2,070 cm^{-1} are attributed to CO adsorption on Ru sites as described above. The two bands at 1,472 cm^{-1} and 1,556 cm^{-1} are assigned to the OCO stretching of bicarbonate and formate species, respectively (8, 42–45), while the peak at 1,622 cm^{-1} likely originates from Ti-OH as a result of surface hydration (8). The reactivity of the formate species is under debate. However, based on the fact that peak intensities at 1,880 to 2,070 cm^{-1} were not affected by the notable accumulation of formate species, we surmise that formate species are only partially dissociated and hydrogenated to CO, which then migrates onto Ru sites to produce methane (45). Overall, these IR signatures are in line with prior literature (8, 25, 42–45), suggesting that CO_2 hydrogenation is facilitated through the formate pathway over Ru/TiO_2 interfaces.

On the other hand, *operando* DRIFT spectra on p-IPOP/Ru/TiO_2 catalyst were notably different. We wish to first emphasize that control experiments with similar conditions were performed with both TiO_2 and p-IPOP encapsulated TiO_2, and the resulting spectra (*SI Appendix*, Fig. S25) were notably different from Fig. 4 *B* and *C*, which confirms that Fig. 4 *B* and *C* represents the unique interface between Ru, IPOP, and TiO_2, denoted as (IPOP)Ru(TiO_2). It was found that a broad band centered at ∼1,910 cm^{-1} quickly emerged upon the introduction of CO_2, together with a weak peak at 2,052 cm^{-1}. As the CO_2 concentration in the DRIFT cell slowly accumulated, the band at 1,910 cm^{-1} gradually evolved and two peaks could be clearly distinguished at steady state at 1,962 cm^{-1} and 1,901 cm^{-1}, which we attribute to CO adsorbed on Ru surface and at the interface [CO-(IPOP)Ru(TiO_2)], respectively. Given the
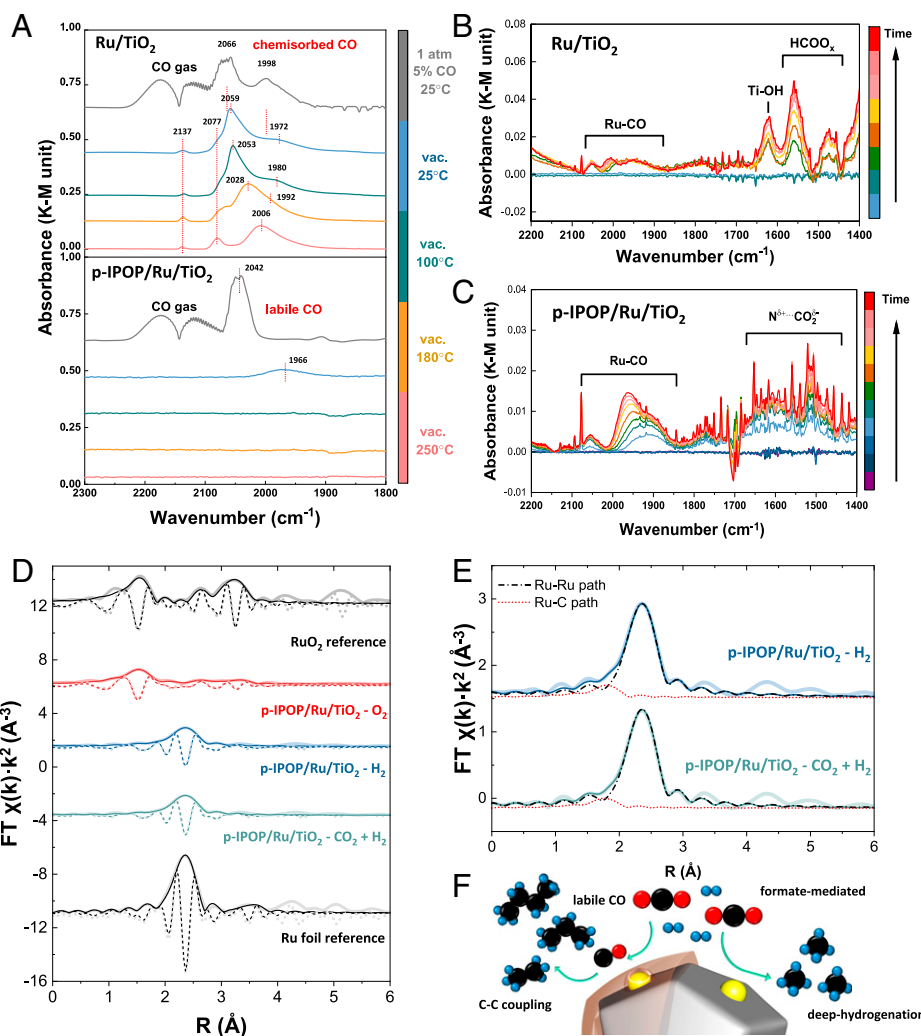
Zhou et al.
Steering CO_2 hydrogenation toward C–C coupling to hydrocarbons using porous organic polymer/metal interfaces

PNAS | 5 of 10
https://doi.org/10.1073/pnas.2114768119

Fig. 4. Mechanistic studies of CO_2 hydrogenation on Ru/TiO_2 and $p\text{-}IPOP/Ru/TiO_2$. (A) DRIFT spectra of CO adsorption on Ru/TiO_2 and $p\text{-}IPOP/Ru/TiO_2$ under different temperature and conditions as indicated in the colored bar on the right. *Operando* DRIFT spectra under CO_2 hydrogenation conditions (250 °C, 20 sccm 75% H_2 + 25% CO_2, 6 bar total pressure) of (B) Ru/TiO_2 and (C) $p\text{-}IPOP/Ru/TiO_2$ catalysts. (D) In situ EXAFS of Ru foil, RuO_2 powder, and p-IPOP/Ru/TiO_2 after oxidative pretreatment, reductive pretreatment, and under reaction conditions (250 °C, 75% H_2 + 25% CO_2). Dark traces are fits; thicker light traces are experimental data; solid traces are magnitudes; dotted traces are imaginary components of the Fourier transform. Data offset for clarity. (E) Comparison of scattering paths of in situ EXAFS from $p\text{-}IPOP/Ru/TiO_2$ after reductive pretreatment and under reaction conditions (250 °C, 75% H_2 + 25% CO_2). Dark traces are fits; thicker light traces are experimental data; dotted traces are fitted scattering paths. (F) Schematic drawing of the reaction intermediates and pathways over Ru/TiO_2 (right) or $p\text{-}IPOP/Ru/TiO_2$ (left) catalysts. Note that atoms are not drawn to scale.

measured CO_2 reaction orders under reaction conditions, it is reasonable to postulate that CO partial pressure rapidly increases as CO_2 accumulates, which leads to an increase of *CO coverage and the consequent increase in IR absorption intensity and shift of the IR band position to higher wavenumbers. The peak at 2,052 cm^{-1}, which did not notably change position, is assigned to $(CO)_n$-$Ru^{\delta+}$, which is known to be coverage-insensitive (40). No distinctive features for carbonates, bicarbonates, and formates were discerned between 1,700 and 1,450 cm^{-1}, and broad bands of relatively low intensity (compared to gaseous water contributions) at 1,513 and 1,610 cm^{-1} were instead observed. We propose that Lewis acid–base interactions between CO_2 and imine groups on the IPOP are responsible for these contributions, given that active sites are surrounded by imino groups in IPOP that can form adducts with CO_2 (19) and that CO_2 can be efficiently activated by Schiff base-modified metals catalysts (18). Interactions between a weak Lewis acid (CO_2) and a weak base (imine) are generally weak. Indeed, instead of strong IR bands in the

region 1,700 to 1,450 cm^{-1}, only a broad feature ranging from 1,700 to 1,550 cm^{-1} over $o\text{-}IPOP/Ru/TiO_2$ was found, and no peaks could be distinguished from $m\text{-}IPOP/Ru/TiO_2$ (*SI Appendix*, Fig. S18). We hypothesize that steric hindrance in the imine bond of the *ortho* isomer dictates a weaker interaction with CO_2 that becomes progressively stronger as the steric hindrance is released moving to the *meta* and *para* isomer. Moreover, the absence of formate intermediates on all encapsulated samples also strongly corroborates the observed transition-state entropic favor induced by IPOP. We hypothesize that the introduction of polymer chains replaces the Ru/TiO_2 interface with a polymer/Ru interface, and the $*HCOO_x$ are no longer abundant on the catalyst surface. Instead, RWGS is likely facilitated from adsorbed CO_2 through N–CO_2 interactions, which has lower configurational entropy in the initial state, resulting in less negative entropic changes.

In situ X-ray absorption near-edge structure and extended X-ray absorption fine structure (EXAFS) data (*SI Appendix*, Figs. S19 and S20) indicate that Ru is completely oxidized to
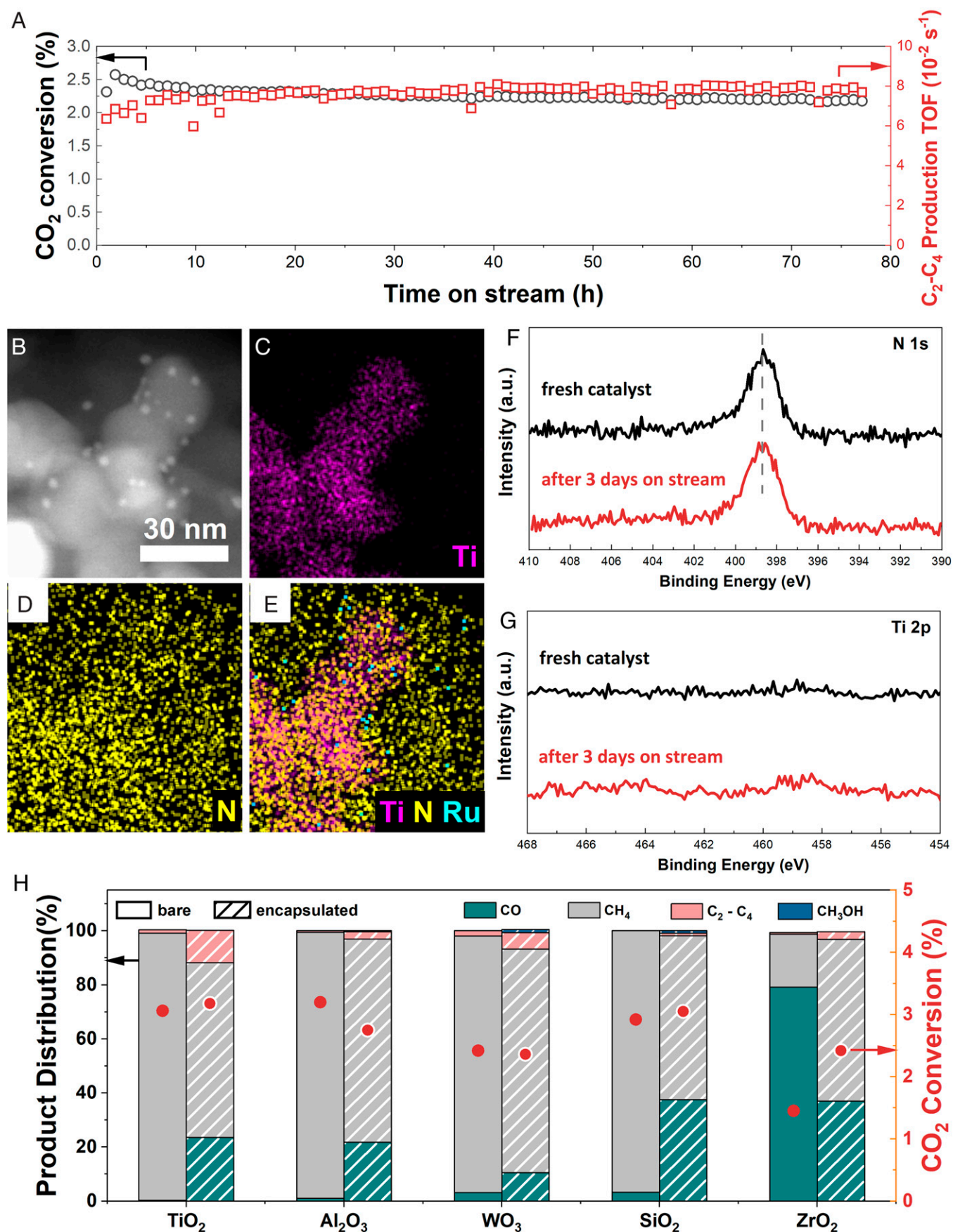
Fig. 5. Study of stability and versatility of the IPOP coating approach. (*A*) Continuous measurement of CO_2 hydrogenation performance of p-IPOP/Ru/TiO_2 at 250 °C, 30 sccm 75% H_2 + 25% CO_2, 6 bar total pressure. (*B*) STEM image and (*C–E*) corresponding EDS maps of several elements in the p-IPOP/Ru/TiO_2 catalyst after the catalytic test reported in *A*. (*F*) N 1s and (*G*) Ti 2p XPS spectra of p-IPOP/Ru/TiO_2 before and after catalytic tests. (*H*) Comparison of CO_2 hydrogenation performance over several Ru-based oxide-supported catalysts either bare or encapsulated within p-IPOP layers.

CHEMISTRY

resemble that of RuO_2 after the oxidation pretreatment and then readily reduced back to metallic state after reduction and also remained metallic during CO_2 hydrogenation. Indeed, the best-fit model of the EXAFS data (Fig. 4D) after oxidation was one that included only Ru–O and Ru–(O)–Ru single scattering paths from RuO_2 (SI Appendix, Table S2). However, for p-IPOP/Ru/TiO_2 after reduction and under reaction conditions (Fig. 4E), it was found that a metallic Ru–Ru path alone does not fully describe the original data, as a misfit persists around $R = 2$ Å for both datasets. An Ru–O scattering path that was initially included to account for Ru–TiO_2 interfacial sites (46, 47) did not improve the fit. Besides, the fitted Ru–O bond (2.19 Å) is significantly longer than theoretical (2.00 Å) or experimental (1.98 Å) values (46). Given that 50% of the Ru atoms are at the Ru particle surface and surrounded by IPOP (SI Appendix, Additional Materials and Methods), Ru–N and Ru–C paths were then considered, and it was found that Ru–C path at 2.22 Å produced the most reasonable fit with the smallest ΔE and reduced χ^2 (SI Appendix, Table S2). Such Ru–C bonding at 2.22 Å is longer than Ru–C carbide bonds (1.98 Å) and instead in agreement with Ru–π bonds in organometallic compounds such as in ruthenocene (2.22 Å) (48). Therefore, we hypothesize that the abundant benzene rings in IPOP are adsorbed face-on onto Ru surfaces, determining the change in reaction selectivity observed for the reaction. Such Ru–C bond most certainly modifies the electronic states of Ru particles as well as break down Ru ensemble size via geometric effects.

In summary (Fig. 4F), kinetic and spectroscopic characterization demonstrates that CO_2 hydrogenation on Ru/TiO_2 mainly produces formate intermediates that are precursors for CH_4, leading to high methanation selectivity. The encapsulation by IPOP overlayer suppressed the reactivity of the Ru/TiO_2 interface while introducing polymer/Ru interface sites, whose selectivity is dominated by *CO intermediates (49). Moreover, IPOP overlayers also greatly reduced *H coverage, which compensated for the decreased number of Ru sites and increased C–C coupling probability and selectivity toward C_{2+} hydrocarbons. We envision that, to further enhance C–C coupling while suppressing methanation, future works should be dedicated to developing new methodologies than can selectively block Ru–TiO_2 interfacial sites without sacrificing Ru–Ru terrace sites.

Stability and Applicability. CO_2 conversion only slightly decreased and hydrocarbon yield increased and stabilized over the course of 3 d on the p-IPOP/Ru/TiO_2 catalyst (Fig. 5A), demonstrating the stability of the sample. STEM and EDS mapping confirmed that the Ru particle size did not appreciably change and that the Ru/TiO_2 was still encapsulated by polymer layers after catalysis (Fig. 5 B–E). XPS analysis also confirmed that no appreciable change was discerned between the fresh and spent catalyst in the N 1s region (Fig. 5F) and that Ti 2p signals were still undistinguishable from the baseline (Fig. 5G), demonstrating maintained encapsulation. IR spectra demonstrated that the imine groups remained stable under catalysis conditions (SI Appendix, Fig. S23). Excellent stability was also found for o-IPOP/Ru/TiO_2 and m-IPOP/Ru/TiO_2 catalysts (SI Appendix, Figs. S21–S23). In summary, the IPOP-coated catalysts demonstrated excellent stability during continuous catalytic tests, with no degradation or decomposition of the IPOP layers.

As a proof of concept of the versatility of the IPOP coating to affect the reactivity of supported catalysts, a series of IPOP-coated Ru catalysts was synthesized using oxide supports including Al_2O_3, WO_3, SiO_2, and ZrO_2 (SI Appendix, Fig. S24) and evaluated for CO_2 hydrogenation. All the corresponding Ru/oxide catalysts produced predominantly methane as product (Fig. 5H), in agreement with previous reports (24, 30, 32, 34,

50), with Ru/ZrO_2 being the only exception and showing prominent RWGS selectivity of 78% possibly due to either strong metal support interactions (51) or Ru redispersion (52). Nevertheless, in all cases it was found that IPOP encapsulation significantly promoted CO production through RWGS pathway and, more importantly, much increased C_{2+} hydrocarbon selectivity. In analogy to the Ru/TiO_2 case, the enhanced CO and C_{2+} production was attributed to the IPOP effect on the Ru surface reactivity and intermediate stability. The fact that product selectivity is also dependent on the nature of the oxide suggests that the support still plays a crucial role in affecting the Ru reactivity through metal–support interactions (28, 34, 53).

Conclusions

We have demonstrated that the CO_2 hydrogenation reaction on supported Ru catalysts is tuned using polymer encapsulation. Specifically, while methanation is predominant over Ru/TiO_2 catalysts, encapsulating the catalyst in imine-based porous polymer layers dramatically altered the reaction selectivity, with notably enhanced CO and C_{2+} hydrocarbons selectivity. Specifically, the TOFs for CO and C_{2+} hydrocarbon production are increased by 80- and 10-fold, respectively. The different kinetic parameters and transition-state entropic gain induced by the IPOP layers suggest that these layers promote different reaction pathways at the polymer/metal interface, as confirmed by *operando* DRIFTS. Given its stability and versatility, we believe the approach of tuning active sites by polymer encapsulation has potential to be applied to a wide range of heterogeneous catalysts. We also envision that the polymer functionality can be systematically designed to interact with specific intermediates and guide novel reaction pathways in complex reaction networks.

Materials and Methods

Synthesis of Hybrid IPOP/Ru/Oxide Catalysts and Postsynthesis Treatments. For encapsulation targeting ~15 nm overlayer thickness, 500 mg of Ru/TiO_2 catalysts (detailed synthesis of Ru nanoparticles and Ru/TiO_2 catalysts can be found in SI Appendix, as well as characterization techniques) together with 290 mg of phthalaldehyde (either ortho-, meta-, or para–) were added into 30 mL of 1,4-dioxane and sonicated for 20 min until full dispersion/dissolution. Five hundred milligrams of 1,3,5-Tris(4-aminophenyl)benzene (TAPB, 97%; TCI) was separately dissolved in 30 mL 1,4-dioxane. The two solutions were then mixed and vigorously stirred for 30 min under room temperature to promote adsorption of organic monomers onto inorganic substrates. Five milliliters of acetic acid was then added as Brønsted acid catalyst for imine condensation. The polymerization was allowed to proceed for 90 min, after which products were collected by centrifugation and subsequently washed with methanol in a Soxhlet extractor for 12 h. The samples were finally dried at 80 °C under dynamic vacuum conditions for 12 h.

The synthesis process to prepare IPOP/Ru/Al_2O_3, IPOP/Ru/WO_3, IPOP/Ru/ZrO_2, and IPOP/Ru/SiO_2 is the same as above, except that 500 mg of either Ru/Al_2O_3, Ru/ZrO_2, or Ru/SiO_2 or 1 g (due to high density and low surface area) of Ru/WO_3 were used, respectively.

Catalytic Measurements. Catalytic experiments were conducted in a custom-made stainless-steel reactor with an internal diameter of 1 cm. Approximately 20 mg of Ru/TiO_2 or 100 mg of IPOP/Ru/TiO_2 were physically mixed with SiC to reach a total mass of 300 mg and loaded into the reactor in between two layers of granular acid-washed quartz. Prior to reaction, the catalysts were activated by oxidation at 250 °C in 5% O_2/Ar atmosphere for 30 min and subsequent reduction at 250 °C in 5% H_2/Ar atmosphere for another 30 min. After pretreatments, the reactant gas mixture (75% H_2 + 25% CO_2) was fed into the reactor at the flow rate of 30 mL·min^{-1}, and the system was gradually pressurized to a total pressure of 6 bar. For steady-state measurements, the reaction was carried out under the condition of 3:1 H_2:CO_2, 250 °C, 6 bar, with gas-hourly space velocity adjusted to maintain CO_2 conversion lower than 5%. All products remained in the gaseous phase and thus continuously analyzed by a GC system equipped with a Hayesep D column and a molecular sieve 5A column. CO and all hydrocarbons were quantified using flame

ionization detector, while H_2 and CO_2 consumption was measured using thermal conductivity detector.

Apparent activation energy measurements were carried out under similar conditions, with 3:1 H_2:CO_2, 6 bar total pressure, varying temperature from 220 °C to 230 °C, 240 °C, and 250 °C while maintaining CO_2 conversion less than 5%.

Rate-order experiments were carried out at 250 °C with constant total flow rate. To obtain rate orders for H_2, the concentration of CO_2 in the reactant feed was kept at 15%, while the concentration of H_2 was gradually increased from 45 to 80% with 4% increments and Ar as balance component. Similarly, to obtain rate order for CO_2, the concentration of H_2 in the reactant feed was kept at 75%, while the concentration of CO_2 was gradually increased from 15 to 25% with 1% increments and Ar as balance component. Throughout all kinetic measurements, the conversions for H_2 and CO_2 were always kept below 5%.

CO_2 conversion was calculated by the equation

$$CO_2 \ conversion \ (\%) = \frac{CO_{2in} - CO_{2out}}{CO_{2in}} \cdot 100\%,$$

where CO_2 (in) and CO_2 (out) denote moles of CO_2 at the inlet and outlet, respectively.

Selectivity distribution of individual products was calculated by equation

$$C_xH_yO_z \ Selectivity \ (\%) = \frac{x \cdot C_xH_yO_{zout}}{CO_{2in} - CO_{2out}} \cdot 100\%,$$

where $C_xH_yO_z$ denote moles of possible products, such as CO, CH_3OH, CH_4, and other hydrocarbons in the outlet.

TOF of individual products was calculated by equation

$$C_xH_yO_z \ TOF \ (s^{-1}) = N_A \ (\cdot mol^{-1}) \cdot CO_2 \ flow \ rate \ (mol \cdot g^{-1} \cdot s^{-1})$$
$$\frac{\cdot yield \ of \ C_xH_yO_z (\%) \cdot x}{Number \ of \ Ru \ sites \ per \ sample \ weight \ (\cdot g^{-1})}.$$

1. H. S. Baker *et al.*, Higher CO_2 concentrations increase extreme event risk in a 1.5°C world. *Nat. Clim. Chang.* **8**, 604–608 (2018).
2. R.-P. Ye *et al.*, CO_2 hydrogenation to high-value products via heterogeneous catalysis. *Nat. Commun.* **10**, 5698 (2019).
3. W. Zhou *et al.*, New horizon in C1 chemistry: Breaking the selectivity limitation in transformation of syngas and hydrogenation of CO_2 into hydrocarbon chemicals and fuels. *Chem. Soc. Rev.* **48**, 3193–3228 (2019).
4. J. Wei *et al.*, Directly converting CO_2 into a gasoline fuel. *Nat. Commun.* **8**, 15174 (2017).
5. P. Gao *et al.*, Direct conversion of CO_2 into liquid fuels with high selectivity over a bifunctional catalyst. *Nat. Chem.* **9**, 1019–1024 (2017).
6. A. A. Peterson, J. K. Nørskov, Activity descriptors for CO_2 electroreduction to methane on transition-metal catalysts. *J. Phys. Chem. Lett.* **3**, 251–258 (2012).
7. J. Pérez-Ramírez, N. López, Strategies to break linear scaling relationships. *Nat. Catal.* **2**, 971–976 (2019).
8. J. C. Matsubu *et al.*, Adsorbate-mediated strong metal-support interactions in oxide-supported Rh catalysts. *Nat. Chem.* **9**, 120–127 (2017).
9. E. D. Goodman, C. Zhou, M. Cargnello, Design of organic/inorganic hybrid catalysts for energy and environmental applications. *ACS Cent. Sci.* **6**, 1916–1937 (2020).
10. R. Alamillo, A. J. Crisci, J. M. R. Gallo, S. L. Scott, J. A. Dumesic, A tailored microenvironment for catalytic biomass conversion in inorganic-organic nanoreactors. *Angew. Chem. Int. Ed. Engl.* **52**, 10349–10351 (2013).
11. T. J. Schwartz, T. S. Wesley, J. A. Dumesic, Modifying the surface properties of heterogeneous catalysts using polymer-derived microenvironments. *Top. Catal.* **59**, 19–28 (2016).
12. T. J. Schwartz *et al.*, Engineering catalyst microenvironments for metal-catalyzed hydrogenation of biologically derived platform chemicals. *Angew. Chem. Int. Ed. Engl.* **53**, 12718–12722 (2014).
13. J. Zhang, S. Deo, M. J. Janik, J. W. Medlin, Control of molecular bonding strength on metal catalysts with organic monolayers for CO2 reduction. *J. Am. Chem. Soc.* **142**, 5184–5193 (2020).
14. B. Zhang *et al.*, Reticular synthesis of multinary covalent organic frameworks. *J. Am. Chem. Soc.* **141**, 11420–11424 (2019).
15. X. Guan *et al.*, Chemically stable polyarylether-based covalent organic frameworks. *Nat. Chem.* **11**, 587–594 (2019).
16. Y. Li *et al.*, Laminated self-standing covalent organic framework membrane with uniformly distributed subnanopores for ionic and molecular sieving. *Nat. Commun.* **11**, 599 (2020).
17. H.-J. Zhu *et al.*, Efficient electron transmission in covalent organic framework nanosheets for highly active electrocatalytic carbon dioxide reduction. *Nat. Commun.* **11**, 497 (2020).
18. Q. Liu *et al.*, Direct catalytic hydrogenation of CO_2 to formate over a Schiff-base-mediated gold nanocatalyst. *Nat. Commun.* **8**, 1407 (2017).
19. C. Villiers, J.-P. Dognon, R. Pollet, P. Thuéry, M. Ephritikhine, An isolated CO_2 adduct of a nitrogen base: Crystal and electronic structures. *Angew. Chem. Int. Ed. Engl.* **49**, 3465–3468 (2010).
20. A. Aitbekova *et al.*, Low-temperature restructuring of CeO2-supported Ru nanoparticles determines selectivity in CO_2 catalytic reduction. *J. Am. Chem. Soc.* **140**, 13736–13745 (2018).
21. L. Grill, S. Hecht, Covalent on-surface polymerization. *Nat. Chem.* **12**, 115–130 (2020).
22. C.-Y. Wu, K.-J. Tu, J.-P. Deng, Y.-S. Lo, C.-H. Wu, Markedly enhanced surface hydroxyl groups of TiO_2 nanoparticles with superior water-dispersibility for photocatalysis. *Materials (Basel)* **10**, 566 (2017).
23. A. R. Bagheri, N. Aramesh, Towards the room-temperature synthesis of covalent organic frameworks: A mini-review. *J. Mater. Sci.* **56**, 1116–1132 (2021).
24. S. Kattel, P. Liu, J. G. Chen, Tuning selectivity of CO_2 hydrogenation reactions at the metal/oxide interface. *J. Am. Chem. Soc.* **139**, 9739–9754 (2017).
25. F. Wang *et al.*, Active site dependent reaction mechanism over Ru/CeO2 catalyst toward CO_2 methanation. *J. Am. Chem. Soc.* **138**, 6298–6305 (2016).
26. A. Kim *et al.*, Selective CO_2 methanation on Ru/TiO2 catalysts: Unravelling the decisive role of the TiO_2 support crystal structure. *Catal. Sci. Technol.* **6**, 8117–8128 (2016).
27. T. Abe, M. Tanizawa, K. Watanabe, A. Taguchi, CO_2 methanation property of Ru nanoparticle-loaded TiO2 prepared by a polygonal barrel-sputtering method. *Energy Environ. Sci.* **2**, 315–321 (2009).
28. X. Li *et al.*, Controlling CO_2 hydrogenation selectivity by metal-supported electron transfer. *Angew. Chem. Int. Ed. Engl.* **59**, 19983–19989 (2020).
29. Y. Yan *et al.*, Ru/Al2O3 catalyzed CO_2 hydrogenation: Oxygen-exchange on metal-support interfaces. *J. Catal.* **367**, 194–205 (2018).
30. M. Cargnello *et al.*, Engineering of ruthenium-iron oxide colloidal heterostructures leads to improved yields in CO_2 hydrogenation to hydrocarbons. *Angew. Chem. Int. Ed. Engl.* **58**, 17451–17457 (2019).
31. H. Yang *et al.*, A review of the catalytic hydrogenation of carbon dioxide into value-added hydrocarbons. *Catal. Sci. Technol.* **7**, 4580–4598 (2017).
32. R. Mutschler, E. Moioli, W. Luo, N. Gallandat, A. Züttel, CO_2 hydrogenation reaction over pristine Fe, Co, Ni, Cu and Al2O3 supported Ru: Comparison and determination of the activation energies. *J. Catal.* **366**, 139–149 (2018).
33. M. S. Duyar, A. Ramachandran, C. Wang, R. J. Farrauto, Kinetics of CO2 methanation over Ru/γ-Al2O3 and implications for renewable energy storage applications. *J. CO2 Util.* **12**, 27–33 (2015).
34. P. Dongapure, S. Bagchi, S. Mayadevi, R. N. Devi, Variations in activity of Ru/TiO2 and Ru/Al2O3 catalysts for CO_2 hydrogenation: An investigation by in-situ infrared spectroscopy studies. *Mol. Catal.* **482**, 110700 (2020).
35. P. Panagiotopoulou, X. E. Verykios, Mechanistic study of the selective methanation of CO over Ru/TiO2 catalysts: Effect of metal crystallite size on the nature of active surface species and reaction pathways. *J. Phys. Chem. C* **121**, 5058–5068 (2017).
36. A. R. Riscoe *et al.*, Transition state and product diffusion control by polymer–nanocrystal hybrid catalysts. *Nat. Catal.* **2**, 852–863 (2019).
37. M. Kuśmierz, Kinetic study on carbon dioxide hydrogenation over Ru/γ-Al2O3 catalysts. *Catal. Today* **137**, 429–432 (2008).
38. S. Saeidi *et al.*, Mechanisms and kinetics of CO_2 hydrogenation to value-added products: A detailed review on current status and future trends. *Renew. Sustain. Energy Rev.* **80**, 1292–1311 (2017).
39. C. S. Kellner, A. T. Bell, Infrared studies of carbon monoxide hydrogenation over alumina-supported ruthenium. *J. Catal.* **71**, 296–307 (1981).
40. F. Solymosi, J. Raskó, An infrared study of the influence of CO adsorption on the topology of supported ruthenium. *J. Catal.* **115**, 107–119 (1989).
41. J. L. Robbins, Chemistry of supported Ru: CO-induced oxidation of Ru at 310 K. *J. Catal.* **115**, 120–131 (1989).

CHEMISTRY

Zhou et al.
Steering CO_2 hydrogenation toward C–C coupling to hydrocarbons using porous organic polymer/metal interfaces

PNAS | 9 of 10
https://doi.org/10.1073/pnas.2114768119

42. L. Proaño *et al.*, In-situ DRIFTS study of two-step CO_2 capture and catalytic methanation over Ru,"Na_2O"/Al_2O_3 Dual Functional Material. *Appl. Surf. Sci.* **479**, 25–30 (2019).

43. X. Wang, Y. Hong, H. Shi, J. Szanyi, Kinetic modeling and transient DRIFTS–MS studies of CO_2 methanation over Ru/Al_2O_3 catalysts. *J. Catal.* **343**, 185–195 (2016).

44. R. A. D. Betta, M. Shelef, Heterogeneous methanation: In situ infrared spectroscopic study of Ru/Al_2O_3 during the hydrogenation of CO. *J. Catal.* **48**, 111–119 (1977).

45. L. Falbo, C. G. Visconti, L. Lietti, J. Szanyi, The effect of CO on CO_2 methanation over Ru/Al_2O_3 catalysts: A combined steady-state reactivity and transient DRIFT spectroscopy study. *Appl. Catal. B* **256**, 117791 (2019).

46. Y. Zhang *et al.*, Tuning reactivity of Fischer–Tropsch synthesis by regulating TiO_x overlayer over Ru/TiO_2 nanocatalysts. *Nat. Commun.* **11**, 3185 (2020).

47. Y. Zhang *et al.*, Ru/TiO_2 catalysts with size-dependent metal/support interaction for tunable reactivity in Fischer–Tropsch synthesis. *ACS Catal.* **10**, 12967–12975 (2020).

48. E. Curis, F. Dubar, I. Nicolis, S. Bénazeth, C. Biot, Statistical methodology for the detection of small changes in distances by EXAFS: Application to the antimalarial ruthenoquine. *J. Phys. Chem. A* **116**, 5577–5585 (2012).

49. T. Avanesian, G. S. Gusmão, P. Christopher, Mechanism of CO_2. reduction by H_2 on Ru(0001) and general selectivity descriptors for late-transition metal catalysts. *J. Catal.* **343**, 86–96 (2016).

50. A. A. Wismeijer, A. P. G. Kieboom, H. Van Bekkum, Selective hydrogenation of citronellal to citronellol over Ru/TiO_2 as compared to Ru/SiO_2. *Appl. Catal.* **25**, 181–189 (1986).

51. Y.-P. Du *et al.*, Engineering the ZrO_2-Pd interface for selective CO_2 hydrogenation by overcoating an atomically dispersed Pd precatalyst. *ACS Catal.* **10**, 12058–12070 (2020).

52. J. Ftouni *et al.*, ZrO_2 is preferred over TiO_2 as support for the Ru-catalyzed hydrogenation of levulinic acid to γ-valerolactone. *ACS Catal.* **6**, 5462–5472 (2016).

53. J. A. H. Dreyer *et al.*, Influence of the oxide support reducibility on the CO_2 methanation over Ru-based catalysts. *Appl. Catal. B* **219**, 715–726 (2017).